

ImplicitTerrainV2: Wavelet-Guided Spatially Adaptive Neural Terrain Representation

Haoan Feng
University of Maryland, College Park
MD, USA
hfengac@umd.edu

Xin Xu
University of Maryland, College Park
MD, USA
xinxu629@umd.edu

Leila De Floriani
University of Maryland, College Park
MD, USA
deflo@umd.edu

Abstract

Digital elevation models (DEMs) underpin terrain analysis in Geographic Information Systems (GIS), but commonly as raster representation, they rely on interpolation for off-grid sampling and finite-difference operators for derivative-based analysis. Implicit neural representations (INRs) offer a continuous alternative, but prior terrain INRs lack explicit frequency control, neglect the gradient structure of terrain, and remain too large and costly to train for practical deployment. We present ImplicitTerrainV2, which advances terrain INRs toward a compact, efficient neural terrain data format by combining a spectral control mechanism with wavelet-guided spatial adaptivity, derivative-aware supervision, and post-training model compression. At its core, a *wavelet complexity field* (WCF) derives spatially-adaptive frequency masks from analytically computed wavelet coefficients, localizing high-frequency capacity to complex terrain regions. The same field guides *complexity-aware adaptive sampling* that concentrates training in high-complexity regions, while *gradient matching* applies extra supervision to enforce the smooth manifold structure of terrain DEMs for improved derivative fidelity. Post-training mixed-precision quantization and entropy coding reduce storage to 1.23 bpp with a 0.28 dB PSNR drop. On 50 Swiss terrain tiles, ImplicitTerrainV2 reaches 66.25 dB end-to-end PSNR, improving over the prior work by 5.70 dB while using 3.2× fewer parameters and training in 55 s per tile on a single GPU. Our compressed neural format is competitive with several established DEM codecs in rate-distortion performance, while additionally supporting off-grid point queries, closed-form derivative evaluation, and resolution-independent reconstruction, which may benefit many downstream GIS applications.

CCS Concepts

• **Information systems** → **Geographic information systems**; • **Computing methodologies** → *Neural networks*; *Shape modeling*.

Keywords

Implicit neural representations, Digital elevation models, Wavelet analysis, Neural terrain representation

1 Introduction

Terrain representation underpins geographic information systems (GIS), supporting applications from hydrology and geomorphology to urban planning and autonomous navigation [39]. The most widely used representation is the digital elevation model (DEM), commonly realized as a regular grid of discrete elevation samples, i.e., raster-DEM. While computationally convenient, raster-DEM imposes inherent limitations: queries between grid points require interpolation; derivative-based quantities such as slope, aspect, and

curvature depend on finite-difference operators. Its accuracy is tied to grid resolution and kernel choice [33, 73]. Additionally, topological analysis on discrete meshes is sensitive to triangulation choices [10, 22]. Standard raster-DEM workflows usually require separate pipelines for each analysis on the decompressed grid, lacking a unified representation that supports continuous evaluation, well-behaved derivatives, and smooth manifold structure.

Implicit neural representations (INRs) encode a signal as a continuous function $f_\theta: (x, y) \mapsto z$ parameterized by a neural network, yielding a compact, resolution-independent, and inherently differentiable model. ImplicitTerrain [23] applied this paradigm to DEM data using a cascaded sinusoidal neural network (SIREN) pipeline that separates smooth shape from geometric detail, enabling topographical analysis and Morse-theoretic topological analysis [52] directly on the learned surface model. However, ImplicitTerrain’s vanilla SIREN architecture has several limitations that prevent it from serving as a practical terrain representation. First, it lacks *spatial frequency localization*, as SIREN neurons contribute globally, high-frequency components needed only near ridgelines or cliffs also activate in smooth regions, a phenomenon termed *frequency leakage* [21]. Second, its value-only supervision does not exploit the terrain’s smooth manifold structure, where well-defined gradients encode physically meaningful shape information. Moreover, its oversized model (3×256 SIREN per stage, $\sim 397K$ parameters) and multi-scale progressive training further limit its practical deployment. These gaps suggest that terrain INRs are not yet viable as a practical data format.

We propose ImplicitTerrainV2, as shown in Fig. 1, which combines wavelet-guided spatial adaptivity, derivative-aware supervision, and post-training model compression to advance terrain INRs toward a compact *neural terrain data format*: a single artifact that couples compact storage, continuous point queries, closed-form derivative evaluation, and resolution-independent reconstruction, targeting offline per-tile encoding settings where these capabilities justify a one-time encoding cost. ImplicitTerrain’s cascaded SIREN architecture is retained, but each per-stage backbone is enhanced through a recent SIREN variant (i.e., TUNER [55]), which provides explicit spectral control. Furthermore, we introduce wavelet-derived spatial masks to localize network frequency components in the spatial domain, as suggested in SASNet [21]. Exploiting the domain gap between RGB images and terrain DEMs, a single scalar complexity field, named *wavelet complexity field* (WCF), is learned from the multi-scale signal analysis results (based on the wavelet analysis). It exploits the containment hierarchy in the spatial distribution across frequency components, generating ordered masks via learned thresholds and producing an interpretable modulation signal for the SIREN backbone.

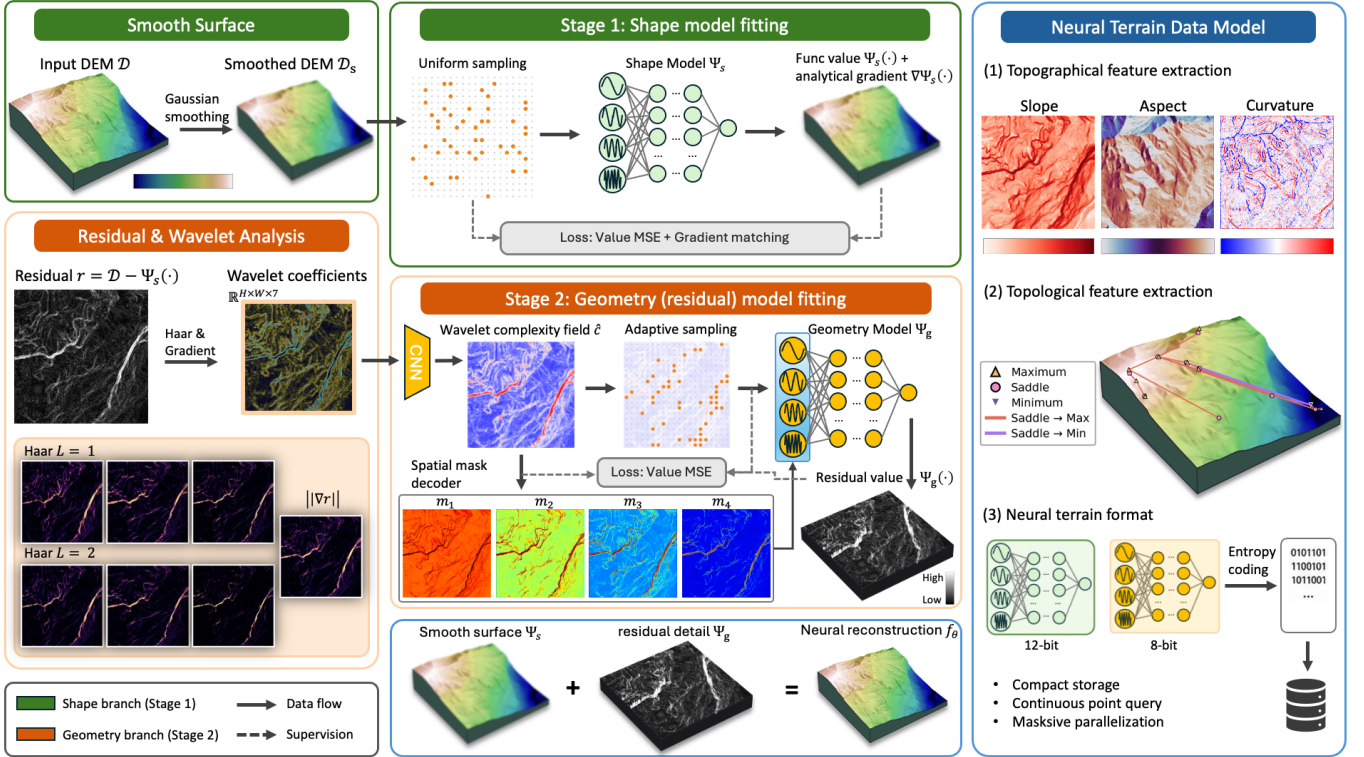


Figure 1: Overview of the ImplicitTerrainV2 pipeline. A terrain DEM is decomposed into a smooth shape model Ψ_s with gradient matching and a residual geometry model Ψ_g with WCF-guided spatial adaptivity. The combined representation supports topological/topographical analysis via analytical gradients, and model compression yields a compact neural terrain data format.

A diverse dataset is curated for the evaluation of ImplicitTerrainV2, which consists of 50 terrain tiles spanning various terrain morphologies. Our ablations isolate the improvements from each module proposed in this work, such as network architecture, hyperparameters, and training strategies. Overall, ImplicitTerrainV2 achieves 66.25 dB end-to-end PSNR with 0.13 m mean absolute error, improving over baseline by +5.70 dB while using $3.2\times$ fewer parameters and requiring 55 s per tile to train on a single GPU. In rate-distortion comparison, the compressed neural format at 1.23 bpp is competitive with several established codecs (Quantize+ZSTD [7], ZFP [42], LERC+ZSTD [7, 14]) in our evaluation. Although SZ3 [40] remains stronger at matched rates, compared to conventional compressed DEMs, the proposed neural representation additionally provides the following capabilities: a closed-form computation of derivatives for topographical features and topological analysis, massive parallelization on modern GPUs, and resolution-independent reconstruction, without requiring separate processing pipelines. Our main contributions are:

- **Wavelet complexity field:** an analytically-derived scalar field summarizing local terrain complexity from gradients and multi-scale wavelet coefficients, from which an ordered family of spatial masks is produced via learned thresholds, outperforming learned hash-grid masks on terrain signals.
- **Gradient matching for terrain INRs:** Hermite-style supervision [32] for the shape model that exploits the smooth

manifold structure of DEMs, improving both elevation and derivative fidelity for downstream analysis.

- **Adaptive sampling:** uniform random subsampling for the shape model and WCF-driven importance sampling for the geometry residual, removing ImplicitTerrain’s multi-scale progressive training without quality loss and reducing the training overhead.
- **Compact neural terrain format:** mixed-precision quantization with entropy coding produces a compact format with competitive rate-distortion performance while retaining INR benefits including continuous surface modeling.

2 Related Work

2.1 Implicit Neural Representations

Implicit neural representations (INRs) parameterize signals as continuous functions $f_\theta: \mathbb{R}^d \rightarrow \mathbb{R}^n$ via neural networks, enabling continuous coordinate queries and inherent differentiability [15]. A central challenge is *spectral bias*: standard ReLU MLPs converge preferentially to low-frequency components, failing to capture fine detail [2, 58, 59]. SIREN [64] mitigates this with periodic sinusoidal activations and a dedicated weight initialization, enabling high-fidelity fitting of images, audio, shapes, and their derivatives, while admitting closed-form gradients and Hessians that are analytically

tractable [56]. Subsequent work broadens spectral coverage via alternative activations such as Gabor wavelets (WIRE) [60], variable-period sinusoids (FINER) [45], and trainable sinusoidal functions (STAF) [16], or use input encoding such as random Fourier features (FFN) [66]. Fourier reparameterization of network weights [63] offers an orthogonal strategy, decomposing weight matrices over fixed Fourier bases without modifying the activation.

A parallel direction augments MLPs with multi-resolution spatial structures. Instant-NGP [53] couples multi-resolution hash grids with a small MLP for fast training, at the cost of large hash tables and no explicit frequency control. ACORN [49] adaptively partitions the spatial domain into individual fitting blocks; BACON [41] constrains each layer to a specific frequency band; and MINER [61] hierarchically tiles the domain, fitting residuals at progressively finer scales. Mixture-of-experts variants partition the domain among specialized sub-networks: LoE [30] tiles position-dependent periodic weights at progressively finer frequencies across MLP layers, while Neural Experts [3] jointly trains a gating network with local experts that dynamically subdivide the domain.

A complementary line targets explicit frequency control and spatial localization. MFN [17] composes networks from multiplicative Fourier or Gabor filters, making the representable spectrum directly inspectable. Yüce *et al.* [72] formalize a sinusoidal network’s representable spectrum as a structured dictionary of sines whose frequencies are integer linear combinations of the first-layer weights; TUNER [55] applies this analysis by freezing SIREN’s first layer with weights drawn from a designed spectral distribution, giving explicit Fourier-grounded control. On the encoding side, spatially-adaptive hash encodings [68] learn per-region masks over multi-resolution hash-grid features, selecting an effective encoding basis as a function of position. Beyond spectral control, Mehta *et al.* [50] modulate SIREN’s periodic activations with an auxiliary network for generalizable local representations, and INCODE [34] further modulates the SIREN backbone via prior-knowledge embeddings from a task-specific harmonizer.

However, controlling *which* frequencies a network can represent does not determine *where* they are spatially active. Because SIREN neurons contribute globally, high-frequency components needed only near complex features also activate in smooth regions, a phenomenon termed *frequency leakage*. SAPE [31], built on FFN [66], progressively activates frequency bands per coordinate during training for implicit spatial adaptation, while SASNet [21] addresses the SIREN case with spatial masks from a hash-grid MLP that modulate neuron activations via element-wise multiplication to suppress unnecessary high-frequency expression. While effective on richly textured signals, learned spatial features such as hash grids may be less well matched to low-frequency dominant, low-contrast signals such as terrain residuals, motivating analytically derived complexity measures as an alternative source of spatial adaptivity.

2.2 Terrain Representation and Analysis

The digital elevation model (DEM) is the dominant terrain representation, usually storing elevation as a regular grid [39]. Triangulated irregular networks (TINs) [27] offer adaptive resolution but require explicit mesh construction, while multi-resolution Gaussian pyramids decompose terrain into frequency bands for progressive

analysis [57]. Common raster- and mesh-based terrain models share a limitation: queries between grid points require interpolation, and derivative quantities depend on the chosen discretization.

Standard topographical features (*e.g.*, slope, aspect, curvature) are computed from DEMs via finite-difference operators [33, 73], whose accuracy is inherently tied to grid resolution and kernel size. Topological analysis provides a complementary, structure-oriented view: Morse theory [52] extracts critical points, separatrix lines, and the Morse–Smale complex from smooth scalar fields, enabling delineation of ridges, valleys, and drainage divides on terrain surfaces. For discrete meshes, Forman’s discrete Morse theory [24, 25] adapts these concepts to simplicial complexes [18–20], with persistence diagrams [26] and the Wasserstein distance [62] providing multi-scale topological summaries. However, discrete methods are sensitive to mesh construction choices such as diagonal selection in grid triangulation [10, 22], motivating continuous representations with well-behaved gradients and Hessians to reduce discretization artifacts in topological extraction.

ImplicitTerrain [23] introduces an INR pipeline for terrain analysis, using a cascaded SIREN in which a surface model fits Gaussian-smoothed data and a geometry model fits the residual, yielding a continuous, differentiable representation that supports Morse-theoretic topological analysis directly on the learned surface. Concurrently, neural elevation models [9] adapt neural radiance fields to produce a differentiable 2.5D height field from imagery for gradient-based path planning. However, existing neural terrain representations lack spatial frequency localization, use value-only supervision without exploiting terrain gradient structure, and do not address model compactness for practical storage and distribution.

2.3 Terrain and Neural Field Data Compression

DEM data is commonly distributed as GeoTIFF [46] with integer quantization. Lossless compression via DEFLATE [11] or Zstandard [7] yields moderate ratios on floating-point elevation data. Kidner and Smith [35] survey DEM-specific techniques including terrain-adapted predictors, and Boucheron and Creusere [4] evaluate wavelet-based lossless DEM compression. In GIS practice, Limited Error Raster Compression [14] (LERC) provides user-controllable per-pixel error bounds and is widely adopted in operational terrain data pipelines.

Scientific compressors [5] optimize different objectives. Transform coding-based methods form one family: ZFP [42] uses orthogonal block transforms with embedded coding for fixed-rate or fixed-accuracy control, while SPERR [38] pairs CDF 9/7 wavelets with SPECK coding. Prediction-based methods form another: SZ [40, 67] excels on spatially smooth data, and FPZIP [43] extends Lorenzo prediction to lossless scientific arrays. HPEZ [44] advances this line with auto-tuned multi-component interpolation. Closer to terrain, Xie *et al.* [70] propose *slope-preserving* lossy compression that prioritizes gradient accuracy over absolute elevation. Although these formats enable efficient storage and, in some cases, block-level random access, their outputs are values alone: gradient computation or topological extraction is left to separate processing pipelines.

Encoding raw data samples as neural network weights and compressing those weights is an emerging paradigm. COIN [12] and COIN++ [13] demonstrate modulation-based INR compression with

meta-learning, while NIRVANA [47] applies quantization-aware training to video INRs. Cool-Chic [37] achieves competitive image compression with lightweight neural decoders, and BRIEF [6] applies INRs for biomedical data. Standard weight compression techniques, including post-training quantization (PTQ), network pruning, and entropy coding [12, 13], provide complementary rate-distortion trade-offs. Unlike traditional formats, a compressed neural representation can retain functional capabilities such as continuous queries and analytical derivative computation, though this potential has not been systematically explored for terrain data.

In summary, prior work separately addresses spectral control and spatial adaptivity in INRs, derivative-based supervision in neural fields, continuous terrain modeling, and compression of rasters or neural network weights. In this work, we bring these threads together in a single terrain representation. Besides, we propose a localized frequency control through a wavelet-derived complexity field, incorporate derivative-aware training tailored to terrain, and apply compact quantized storage, while supporting continuous evaluation and derivative queries directly from the stored representation.

3 Method

We assume the underlying terrain surface is a continuous function $f : \mathbb{R}^2 \rightarrow \mathbb{R}$ that maps normalized coordinates $(x, y) \in [0, 1]^2$ to elevation z , of which a terrain tile DEM $\mathcal{D} \in \mathbb{R}^{H \times W}$ is a discrete sampling at grid points. We seek a neural approximation f_θ of f whose grid-point values reconstruct \mathcal{D} and that provides resolution-independent continuous point queries, analytical differentiability, and continuous shape analysis without discretization. Figure 1 illustrates the full ImplicitTerrainV2 pipeline.

3.1 Network Architecture

Our terrain representation is a cascade of two frequency-controlled SIREN networks with input-layer spatial masking. A *shape model* Ψ_s fits a Gaussian-smoothed version of the DEM D_s and captures the large-scale smooth manifold, while a *geometry model* Ψ_g fits the full-resolution residual $r = \mathcal{D} - \Psi_s(\cdot)$ and recovers fine-scale detail; the final reconstruction is $f_\theta(x, y) = \Psi_s(x, y) + \Psi_g(x, y)$.

Each stage is a SIREN [64] tailored to terrain fitting by two design choices: (i) for Ψ_s and Ψ_g , a *frozen first layer* that acts as a designed Fourier basis, providing explicit spectral control over the network’s representable frequencies, and (ii) for Ψ_g , an input-layer *spatial mask* derived from a wavelet-analytic complexity signal, localizing those frequencies to the terrain regions that need them. The SIREN backbone is retained because any derivative of a sinusoid remains a sinusoid, so the network yields smooth and analytically tractable derivatives at all orders, a property important for the topographical and topological terrain analysis we target [23, 56].

Let $\mathbf{x} = (x, y) \in [0, 1]^2$ be the normalized input coordinate and L the number of hidden layers. Each stage computes:

$$\begin{aligned} \mathbf{h}_1(\mathbf{x}) &= \sin(\omega_0 (\mathbf{W}_0 \mathbf{x} + \mathbf{b}_0)) \odot \mathcal{M}(\mathbf{x}), \\ \mathbf{h}_{l+1}(\mathbf{x}) &= \sin(\omega_0 (\mathbf{W}_l \mathbf{h}_l + \mathbf{b}_l)), \quad l = 1, \dots, L-1, \\ f_\theta(\mathbf{x}) &= \mathbf{W}_L \mathbf{h}_L + b_L, \end{aligned} \quad (1)$$

where ω_0 is the frequency scaling factor, $\{\mathbf{W}_l, \mathbf{b}_l\}_{l=0}^L$ are the layer weights and biases, and \odot denotes element-wise multiplication between the first-layer activations and a per-neuron spatial mask $\mathcal{M}(\mathbf{x}) \in [0, 1]^n$, with n the width of the first layer. The same formulation covers both stages: the geometry model uses a non-trivial WCF-derived mask (Sec. 3.2), whereas the shape model sets $\mathcal{M}(\mathbf{x}) \equiv 1$, since its smoothed target contains no spatially localized high-frequency content to gate, so Eq. 1 reduces to a standard frequency-embedded SIREN for Ψ_s . The first-layer parameters $\mathbf{W}_0 \in \mathbb{R}^{n \times 2}$ and $\mathbf{b}_0 \in \mathbb{R}^n$ are frozen at initialization and determine the representable spectrum of the network, while \mathcal{M} localizes that spectrum in space. All other weights and biases are trained jointly.

Yüce *et al.* [72] showed that every hidden neuron of a SIREN can be expanded as a sum of sines whose frequencies are integer linear combinations of the rows of \mathbf{W}_0 : for a 2D input, the set $\{\mathbf{k}^\top \mathbf{W}_0 : \mathbf{k} \in \mathbb{Z}^n\}$ defines the network’s representable 2D spectrum. This recasts the first layer as a frequency embedding whose frequencies, motivated by the Fourier analysis of bandlimited 2D elevation signals, can be sampled directly on the integer frequency lattice. Following TUNER [55] and SASNet [21], we set the rows of \mathbf{W}_0 to 2D frequency vectors $\omega_i \in \mathbb{Z}^2$ drawn from an integer frequency grid, and we sample the phases \mathbf{b}_0 uniformly in $[0, 2\pi)$. The n rows are partitioned into $K + 1$ frequency bands by magnitude: band 0 collects the low-frequency rows satisfying $\|\omega_i\|_\infty \leq \mathcal{L}$, and bands $1, \dots, K$ cover the higher-frequency region from the low-range \mathcal{L} up to a bandlimit \mathcal{B} , with each band corresponding to a contiguous range of frequencies. This construction makes the representable spectrum explicit and reproducible, rather than leaving it to emerge implicitly from random initialization as in standard SIREN.

For spatially-adaptive masking, let $\mathbf{W}_0^{(i)}$ denote the rows of \mathbf{W}_0 assigned to frequency band i , with $i = 0$ the low-frequency band and $i = 1, \dots, K$ the higher-frequency bands. Given per-band scalar masks $m_i(\mathbf{x}) \in [0, 1]$, whose construction from the wavelet complexity field is described in Sec. 3.2, we form the per-neuron mask \mathcal{M} by tiling $m_i(\mathbf{x})$ across every neuron in band i :

$$\mathcal{M}(\mathbf{x}) = \left[\underbrace{m_0(\mathbf{x}), \dots, m_0(\mathbf{x})}_{|\mathbf{W}_0^{(0)}|}, \underbrace{m_1(\mathbf{x}), \dots, m_1(\mathbf{x})}_{|\mathbf{W}_0^{(1)}|}, \dots \right]^\top, \quad (2)$$

and apply it element-wise to the first-layer activations as in Eq. 1. The low-frequency band is always active ($m_0 \equiv 1$); only the K higher-frequency bands are gated. In practice, spatial masks are applied to a group of neurons through broadcasting in PyTorch for efficiency. This band-wise masking structure is adopted from SASNet [21]; our departure lies in how $\{m_i\}$ are produced. SASNet generates them with a multi-scale hash-grid MLP trained jointly with the SIREN, a design that benefits from rich spatial texture in natural images but tends to collapse on the smoother, lower-contrast terrain residuals (Fig. 2). We replace the hash-grid branch with a *wavelet complexity field* (Sec. 3.2) that derives $\{m_i\}$ from analytically computed wavelet coefficients of the input terrain, providing an interpretable mask signal grounded in the multi-scale frequency content of the data itself. Masks are applied only at the first layer; hidden-layer masks, used by SASNet for images, degrade terrain fitting and are therefore omitted (see Supp. B).

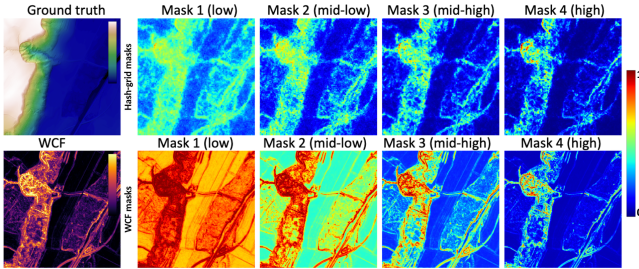


Figure 2: Mask comparison on a terrain tile. Hash-grid masks (top) are spatially noisy and lack interpretability, failing to distinguish complex from simple regions. WCF masks (bottom) show a clear spatial structure with a containment hierarchy from low to high frequency bands.

3.2 Wavelet Complexity Field (WCF)

WCF produces the geometry model’s K per-band spatial masks $\{m_i\}$ from a single scalar complexity field, computed by a lightweight CNN decoder over analytical multi-scale wavelet features of the input and sliced into K nested masks by K strictly ordered thresholds. The masks gate the geometry model’s first-layer frequencies (Eq. 1), localizing high-frequency capacity to complex terrain regions.

Wavelet coefficients decompose a 2D signal into multi-scale frequency components while preserving spatial localization, with large-magnitude coefficients indicating rapid spatial variation at that scale and location [4, 48]. Computing them analytically from the input terrain makes the complexity signal available before optimization. SASNet’s hash-grid masks, by contrast, have no analytical form and are jointly trained with the SIREN under the geometry model’s residual reconstruction loss; since this residual is itself the geometry model’s fitting target, the masks must be inferred from the same smooth, low-contrast signal they are meant to gate, which causes them to degrade on post-shape residuals (Fig. 2).

To turn the complexity field into the K per-band masks, we exploit the *containment hierarchy* reported by SASNet [21] for well-learned image masks: the active region of each higher-frequency band is contained in that of the lower-frequency bands, since regions requiring fine detail often also require coarser content. We find this hierarchy is also important for stable terrain optimization. We therefore derive all K masks from the WCF (a single scalar field) through K ordered thresholds, which ensures containment by construction and reduces the decoder to a scalar-valued regression.

We compute the stationary wavelet transform (SWT) [54] of residual r at $L = 2$ levels with Haar wavelets; the SWT is shift-invariant and preserves spatial resolution at every level by omitting downsampling. This yields six absolute-valued detail coefficients $\{|d_h^{(\ell)}|, |d_v^{(\ell)}|, |d_d^{(\ell)}|\}_{\ell=1}^L$ encoding horizontal, vertical, and diagonal frequency content at each coordinate. We append the local gradient magnitude $\|\nabla r\|$ as a seventh first-order channel, stack into $\mathbf{F}(r) \in \mathbb{R}^{7 \times H \times W}$, and z-score normalize each channel to obtain $\bar{\mathbf{F}}(r)$.

A CNN decoder g_ϕ then maps $\bar{\mathbf{F}}(r)$ to a scalar field on a low-resolution grid, which is per-tile instance normalized to obtain the complexity field \hat{c} :

$$c = g_\phi(\bar{\mathbf{F}}(r)), \quad \hat{c}(\mathbf{x}) = (c(\mathbf{x}) - \mu_c) / (\zeta_c + \epsilon), \quad (3)$$

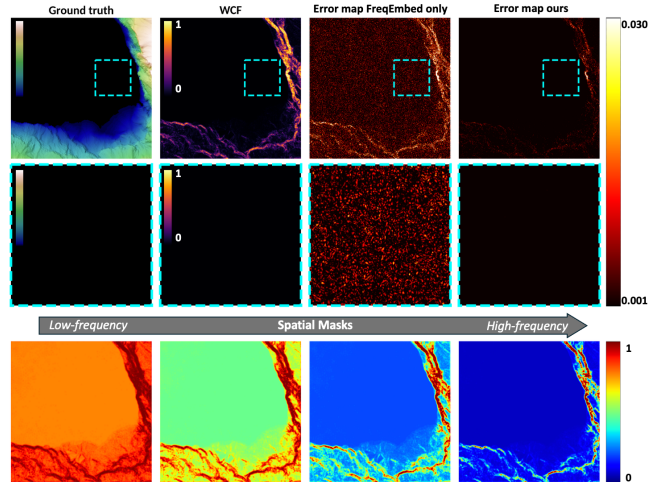


Figure 3: Frequency leakage in the geometry model. Without spatial masks (bottom row), high-frequency neurons introduce spurious oscillations in flat regions. WCF masks (second column) localize errors to complex terrain. The middle row zooms into a flat region (cyan box), where WCF masks reduce mean error by 80.5%.

where μ_c, ζ_c are the spatial mean and standard deviation of c over the tile. The two normalizations play complementary roles: the per-channel z-scoring of $\mathbf{F}(r)$ balances the magnitudes of the wavelet feature channels before the decoder, while the per-tile instance normalization of c standardizes the threshold operating range so a single learned set of $\{\tau_i\}$ generalizes across tiles with different elevation ranges.

We map \hat{c} to K soft per-band masks through K strictly ordered thresholds $\tau_1 < \dots < \tau_K$:

$$m_i(\mathbf{x}) = \sigma(\hat{c}(\mathbf{x}) - \tau_i), \quad (4)$$

where σ is the sigmoid. To enforce strict ordering without constrained optimization, we adopt a cumulative-softplus reparameterization:

$$\tau_1 = \tilde{\tau}_1, \quad \tau_i = \tau_{i-1} + \text{softplus}(\delta_i), \quad i = 2, \dots, K, \quad (5)$$

where $\text{softplus}(\delta_i) = \log(1 + e^{\delta_i})$, and $\{\tilde{\tau}_1, \delta_2, \dots, \delta_K\}$ are learnable scalars that parameterize the thresholds $\{\tau_i\}$ filtering $\hat{c}(\mathbf{x})$: $\tilde{\tau}_1$ sets the lowest threshold, and each δ_i controls the gap between consecutive thresholds. Each step adds a positive $\text{softplus}(\delta_i)$, so $\tau_i > \tau_{i-1}$ by construction. Higher thresholds suppress more locations, so the active regions of the masks form a nested chain: the lowest band is active almost everywhere, the highest only on the most complex features. The K masks are tiled across the corresponding neuron groups of \mathbf{W}_0 via Eq. 2.

Spatial masking is essential because SIREN neurons act globally over the input domain: without it, high-frequency components needed only in complex regions produce spurious oscillations in flat areas (Fig. 3). Empirically (Sec. 4.2), the frequency embedding alone yields no improvement on the geometry stage, while adding WCF masks recovers +2.64 dB and reduces mean error in the high-lighted flat region by 80.5%. WCF masks also display the expected containment hierarchy (Fig. 2), with mean activation decreasing

monotonically from 0.82 in the lowest band to 0.13 in the highest, concentrating high-frequency capacity on ridgelines and sharp slope transitions.

3.3 Gradient Matching

Supervising both function values and their derivatives, known as Sobolev training [8], improves data efficiency and generalization in neural networks, and has been applied in INRs through Eikonal constraints for signed distance functions [29] and approximated image derivatives [71]. However, derivative supervision remains uncommon in general neural field training, as many signals lack well-defined or easily computable ground-truth gradients. Terrain DEMs are a notable exception: the elevation function over a smooth manifold has first-order partial derivatives ($\partial f_\theta/\partial x, \partial f_\theta/\partial y$) that correspond directly to physical slope components, are computable from the DEM via finite differences, and are essential for downstream geospatial analysis. We exploit this structure through *gradient matching*, a Hermite-style [32] loss $\mathcal{L}_{\text{MSE}} + \lambda \cdot \mathcal{L}_{\text{grad}}$ that supervises both function values and derivatives:

$$\mathcal{L}_{\text{MSE}} = \frac{1}{N} \sum_{i=1}^N (f_\theta(x_i, y_i) - f_i)^2 \quad (6)$$

$$\mathcal{L}_{\text{grad}} = \frac{1}{M} \sum_{j=1}^M \|\nabla f_\theta(x_j, y_j) - \nabla f_j\|^2 \quad (7)$$

The gradient targets ∇f_j are pre-computed from the DEM using central finite differences, and ∇f_θ is obtained via automatic differentiation through the SIREN network. We set $\lambda = 0.1$ to keep the gradient term on a comparable scale to \mathcal{L}_{MSE} on normalized elevation, and randomly subsample $M = 10,000$ coordinates per batch for gradient supervision to limit computational overhead (see Sec. C for cost analysis).

Gradient matching increases the effective supervision density: each training coordinate provides one value constraint and two first-order derivative constraints, adding complementary geometric information per sample. For terrain, these derivative constraints are particularly informative because the elevation surface is smooth and its gradients encode physically meaningful local geometry (*i.e.*, slope direction and magnitude) that pure MSE fitting loss must infer indirectly from neighboring point values.

Gradient matching also complements the frequency embedding layer: while the frequency embedding broadens the network’s *spectral* capacity by covering more Fourier frequencies, gradient supervision provides denser *spatial* constraints that guide the network to allocate these components accurately across the terrain surface. We apply gradient matching only to the shape model Ψ_s , because it fits the smooth manifold where gradients are spatially coherent and physically meaningful (*e.g.*, terrain slope). Together, as shown in Sec. 4.4, the two mechanisms address frequency coverage and spatial fidelity from complementary directions.

3.4 Efficient Training and Inference

A practical neural terrain format must be efficient to train and to query. We address training cost from three aspects: (i) adaptive coordinate sampling, (ii) analytical gradient inference that leverages SIREN’s differentiable structure as a built-in capability of the

representation, and (iii) mixed-precision computation with kernel compilation that accelerates both training and inference.

Adaptive sampling. Previous work (ImplicitTerrain) training uses all grid coordinates, treating all spatial locations equally at each iteration. For terrain, this is inefficient because in flat regions, the model converges faster and does not benefit from dense sampling, while in complex regions (*e.g.*, ridgelines, cliffs), it requires concentrated optimization effort.

We use different sampling strategies for the two stages, matched to the spectral character of each target. For the shape model, whose target is the band-limited smoothed manifold, we apply simple uniform random subsampling of the 500×500 grid at each iteration. For the geometry model, whose target is the high-frequency residual with strongly non-uniform spatial importance, we exploit the normalized WCF complexity field $\hat{c}(x, y)$ as an importance map and sample training coordinates from a mixture distribution:

$$p(x, y) = (1 - \alpha) \cdot \mathcal{U} + \alpha \cdot \hat{c}^+(x, y) / \sum \hat{c}^+, \quad (8)$$

where $\hat{c}^+ = \max(\hat{c}, \epsilon_s)$ is the rectified normalized complexity (with $\epsilon_s > 0$ ensuring minimum coverage of all regions), \mathcal{U} is the uniform distribution over the grid, and $\alpha = 0.75$ controls the adaptive fraction. Sample indices are drawn per iteration on the CPU in parallel with GPU training to avoid sampling overhead.

Empirically, both strategies provide substantial speedups at negligible quality cost. For the shape model, 25% uniform subsampling incurs only -0.01 dB PSNR loss while providing a $1.84\times$ training speedup (Supp. C); the smooth manifold tolerates aggressive subsampling because the target is band-limited and spatially redundant. For the geometry model, complexity-guided sampling slightly improves fitting quality ($+0.53$ dB) while being $2.25\times$ faster, as the network concentrates optimization effort on regions that need it most. Combined with the cascaded architecture, adaptive sampling also removes the need for ImplicitTerrain’s multi-scale progressive training: a single-resolution pass suffices and yields $+3.42$ dB higher end-to-end PSNR at $1.57\times$ faster wall-clock time (Supp. C).

Analytical gradient queries. At inference time, WCF masks are precomputed and frozen, so the model reduces to a masked SIREN with fixed per-location gains. A key advantage of this model is that spatial derivatives can then be computed analytically via the chain rule through SIREN layers, without constructing a computational graph [56]. For a SIREN hidden layer $\mathbf{h}_{l+1} = \sin(\omega_0(\mathbf{W}_l \mathbf{h}_l + \mathbf{b}_l))$, the Jacobian with respect to the layer input is:

$$\frac{\partial \mathbf{h}_{l+1}}{\partial \mathbf{h}_l} = \omega_0 \cdot \text{diag}(\cos(\omega_0(\mathbf{W}_l \mathbf{h}_l + \mathbf{b}_l))) \cdot \mathbf{W}_l. \quad (9)$$

To avoid the overhead of PyTorch’s autograd backward, we implement Eq. 9 explicitly. The forward pass caches each layer’s cosine pre-activation $\cos(\omega_0(\mathbf{W}_l \mathbf{h}_l + \mathbf{b}_l))$. A manual chain-rule pass propagates the running 2D input gradient through the frozen weights $\{\mathbf{W}_l\}$, scaled element-wise by the cached cosines, producing $\partial f_\theta/\partial x$ and $\partial f_\theta/\partial y$ alongside f_θ in a single call. At equal FLOP count to autograd, this manual chain has no graph-construction or dispatch overhead and can be fused end-to-end into a single GPU kernel. Moreover, these quantities are resolution-independent: they can be evaluated at any continuous coordinate without resampling or grid construction, unlike finite-difference computation on discrete

DEMs, which is inherently tied to grid resolution. These properties make the neural terrain format a continuous, smooth surface manifold whose analytical derivatives directly support downstream topographical and topological analysis, allowing it to serve as both a data store and an analysis tool.

Mixed-precision computation and compilation. We accelerate both training and inference using automatic mixed precision (AMP) [51] and kernel compilation via `torch.compile` [1]. AMP performs most arithmetic in float16 while keeping master weights and numerically sensitive operations (e.g., reductions, normalization) in float32, reducing memory bandwidth and compute cost without sacrificing training stability. Kernel compilation fuses operation sequences into optimized GPU kernels, substantially reducing Python interpreter overhead and the cost of managing the autograd computational graph. This compilation step is important for analytical gradient queries: the analytical formulation has the same FLOP count as autograd, and without compilation the speedup is marginal (1.06 \times); with compilation, the fused forward-and-gradient kernel achieves 4.63 \times speedup, reaching 77.3 M queries/s for simultaneous elevation and gradient evaluation (Sec. 4.3).

3.5 Model Compression

For the neural terrain representation to be practical as a data format, the trained weights must be compressed for storage and distribution. We apply a standard two-stage neural-weight compression pipeline [28]: post-training quantization (PTQ) of the float32 weights to low-bit integers, followed by lossless entropy coding of the quantized symbol stream. Both stages operate on the trained model and add no per-tile training cost.

PTQ converts the trained float32 weights to a lower-precision integer representation after training, without any additional retraining loop [28]. For a weight tensor \mathbf{W} at bit-width b , we compute a scale $s = \max(|\mathbf{W}|)/(2^{b-1} - 1)$ and round each entry to the nearest signed b -bit integer \mathbf{W}_{int} ; at inference the integer weights are dequantized as $\hat{\mathbf{W}} = s \mathbf{W}_{\text{int}}$ for computation, while only \mathbf{W}_{int} and s are stored on disk. We use symmetric uniform weight-only quantization, with per-output-channel scales for weights and per-tensor scales for biases; the frozen frequency-embedding layer \mathbf{W}_0 is reproducible from its initialization seed and is not stored. A per-layer sensitivity sweep (Supp. D) shows that the two cascade stages have different bit-width tolerances: the shape model Ψ_s requires $b = 12$ to preserve gradient accuracy for downstream topographical and topological analysis, whereas the geometry model Ψ_g and the WCF decoder tolerate $b = 8$ with negligible PSNR loss. We therefore adopt a mixed-precision configuration of $b = 12$ for Ψ_s and $b = 8$ for Ψ_g and the WCF decoder.

After PTQ, the integer weight values are not uniformly distributed, with low-magnitude values far more common than extreme ones, leaving headroom for additional lossless compression. We compress the quantized weight stream with arithmetic coding [69], which encodes a sequence of symbols as a single fractional number whose code length approaches the empirical entropy of the symbol distribution. Beyond the network weights, the WCF mask generator at inference also requires the per-tile complexity field \hat{c} that produces the band masks through the learned thresholds. We store this field at the low resolution at which it is produced (the

same grid used for bilinear interpolation during training), uniformly quantized to 4 bits and entropy-coded with the same arithmetic coder. The stored artifact per tile thus consists of the entropy-coded integer weight stream, per-channel scales, the learned thresholds and normalization statistics, and the entropy-coded low-resolution complexity field.

We use PTQ over quantization-aware training (QAT), as our ablation (Supp. D) shows that QAT yields negligible quality improvement while substantially complicating training. Rate-distortion results, including comparisons against established codecs, are reported in Sec. 4.3.

4 Experiments

4.1 Experimental Setup

For evaluation, we curated a 50-tile terrain dataset from SwissTopo’s swissALTI3D [65], a high-resolution LiDAR-derived DEM of Switzerland. Each processed tile covers 1000×1000 pixels at 1 m resolution. The resulting set spans alpine ridges, glacial valleys, plateaus, and mixed terrain, with elevation ranges from 101 m to 1,668 m. Details of the curation pipeline are provided in Supp. A.

We compare ImplicitTerrainV2 with three neural terrain representations: (1) **ImplicitTerrain** [23], a cascaded SIREN baseline with three 256-unit hidden layers and $\omega_0 = 30$; (2) **ImplicitTerrain-128**, the same baseline reduced to a 3×128 SIREN backbone for an architecture-matched comparison; and (3) **SASNet** [21], which augments a 3×128 SIREN backbone with multi-scale hash-grid masks. For compression evaluation, we additionally compare against several widely-used classical terrain formats (see Sec. 4.3).

Both stages of ImplicitTerrainV2 use $L = 3$ hidden SIREN layers with width 128. The shape model uses $\omega_0 = 30$ with a low-frequency-only frequency embedding ($\mathcal{L} = 10, K = 0$), matching the spectral content of the smoothed terrain; no spatial masking is applied ($\mathcal{M} \equiv \mathbf{1}$). The geometry model uses $\omega_0 = 150$ with a 50%/50% low/high-frequency neuron split ($\mathcal{L} = 6, K = 4$ higher-frequency bands up to bandlimit $\mathcal{B} = 40$); its WCF masks gate the K higher-frequency bands per spatial location and are produced from Haar SWT at two decomposition levels, decoded by a 3-layer CNN ($7 \rightarrow 48 \rightarrow 48 \rightarrow 1$). This configuration reduces ImplicitTerrain’s 3×256 backbone, yielding a more compact neural terrain format. Model sizes were selected through a preliminary search to balance parameter count, training/inference speed, and fitting quality.

All models are optimized with Adam [36] at a learning rate of 10^{-4} . The shape model trains for 3,000 iterations on 500×500 Gaussian-smoothed terrain ($\sigma = 4.0$), and the geometry model trains for 2,000 iterations on 1000×1000 normalized residuals; the per-stage ω_0 values above were selected through hyperparameter search. Gradient matching ($\lambda = 0.1, M = 10,000$ subsampled coordinates) and adaptive sampling ($\alpha = 0.75$, geometry model only) are applied to ImplicitTerrainV2 and, where compatible, to SASNet; the SIREN-based ImplicitTerrain baselines retain their original training recipe without these additions. Training runs with `torch.compile` and AMP on a single NVIDIA RTX A5000 GPU.

We report peak signal-to-noise ratio (PSNR) computed on per-tile min-max-normalized elevations in $[0, 1]$, mean absolute error

Table 1: Main fitting results on 50 tiles, best per column in bold. E2E PSNR (mean \pm std) is computed on the full cascaded reconstruction. MAE and MaxAE are scaled back to the original elevation scale. Peak Mem is the peak GPU memory during training, and Geo-Iter is the per-iteration wall-clock time of the geometry model, which is the training bottleneck.

Method	Params	E2E PSNR (dB) \uparrow	MAE (m) \downarrow	MaxAE (m) \downarrow	Peak Mem (GB) \downarrow	Geo-Iter (ms) \downarrow
ImplicitTerrain [23]	397K	60.55 \pm 5.67	0.197	29.73	9.8	81.9
ImplicitTerrain-128	100K	49.74 \pm 5.34	1.436	32.46	4.9	34.5
SASNet [21]	139K	64.48 \pm 4.27	0.125	17.56	5.4	41.3
ImplicitTerrainV2	124K	66.25 \pm 4.09	0.132	11.85	1.7	20.2

(MAE) and maximum absolute error (MaxAE) in meters after rescaling to each tile’s original elevation range, and per-iteration wall-clock time to characterize training throughput. For the shape model, we additionally report gradient MAE (GradMAE), defined as

$$\text{GradMAE} = \frac{1}{N} \sum_{i=1}^N \|\nabla \Psi_s(\mathbf{x}_i) - \widehat{\nabla f}(\mathbf{x}_i)\|_1, \quad (10)$$

where $\widehat{\nabla f}$ denotes the ground-truth gradient obtained via central finite differences on the DEM and the average is taken over all N grid coordinates. GradMAE quantifies derivative fidelity, which is essential for the downstream terrain analysis tasks in Sec. 4.5.

4.2 Terrain Fitting Results

Table 1 compares ImplicitTerrainV2 against baseline methods on all 50 tiles. We report end-to-end (E2E) PSNR, computed on the full cascaded reconstruction $\hat{z} = \Psi_s + \Psi_g$ against the ground-truth DEM, so it reflects the combined fidelity of the shape and geometry stages rather than either stage in isolation. ImplicitTerrainV2 achieves 66.25 dB E2E PSNR, improving over ImplicitTerrain by +5.70 dB at 3.2 \times fewer parameters and 5.8 \times lower peak GPU memory. Against SASNet, ImplicitTerrainV2 gains +1.77 dB and reduces worst-case error by 33% (11.85 vs. 17.56 m) while running 2.0 \times faster per iteration. SASNet attains a slightly lower MAE (0.125 vs. 0.132 m), likely a consequence of its larger auxiliary masking module (39K vs. 24K parameters for WCF) that can fit localized outliers more aggressively; we prioritize PSNR and MaxAE as the primary metrics since they better reflect worst-case fidelity for downstream analysis.

Figure 4 provides a qualitative comparison across three representative tiles. ImplicitTerrainV2 concentrates residual errors on complex features, leaving flat and smooth regions with minimal error, illustrating the effect of WCF-guided frequency allocation. The frequency-domain error maps in the last column show systematic directional streaks for ImplicitTerrain, indicating missing or poorly fitted frequency components. These artifacts are alleviated in ImplicitTerrainV2’s reconstruction, supporting the interpretation that the frequency embedding and WCF masks achieve broader and more accurate spectral coverage.

Since downstream terrain analysis hinges on the shape model’s derivative accuracy, we also evaluate gradient fidelity in isolation (Tab. 2). Gradient matching (GM) reduces GradMAE by 6.4 \times and worst-case elevation error by 7.7 \times over the SIREN baseline. Combining the frequency embedding (FreqEmbed) with GM yields the best results across all metrics, confirming their complementary contributions to elevation and derivative accuracy.

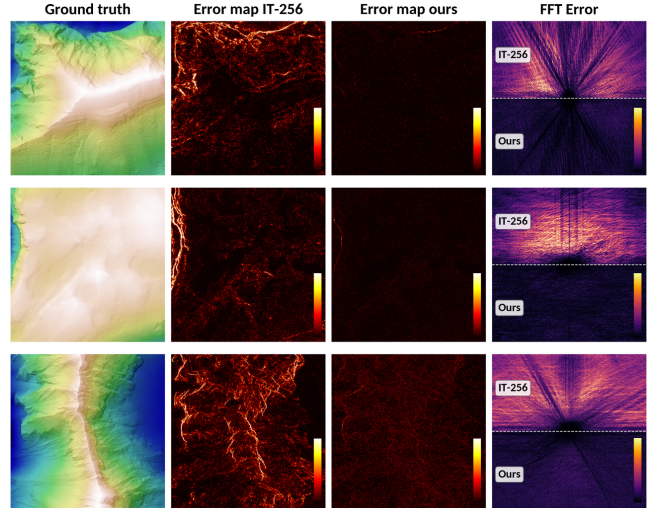


Figure 4: Qualitative comparison on three terrain tiles. The 2nd and 3rd columns show spatial error maps for ImplicitTerrain and ImplicitTerrainV2 (hot colormap for the absolute error up to 1.25% of the input elevation), while the 4th column shows the frequency-domain error map comparison.

Table 2: Shape model fitting quality and gradient fidelity. GradMAE measures the mean absolute error of the predicted gradient field against the finite-difference ground truth.

Shape Config	PSNR (dB) \uparrow	GradMAE \downarrow	MaxAE (m) \downarrow
SIREN	55.50 \pm 2.80	0.097	10.52
+GM	67.26 \pm 1.24	0.024	1.84
+FreqEmbed	59.81 \pm 1.93	0.086	7.93
+FreqEmbed+GM	70.54 \pm 1.89	0.015	1.37

4.3 Storage Efficiency and Inference

Beyond fitting quality, we evaluate ImplicitTerrainV2 as a terrain data format in terms of storage cost, measured in bits per pixel (bpp, encoded bits divided by the number of DEM grid cells), and query performance. Table 3 compares ImplicitTerrainV2 against traditional terrain compression methods. At the recommended 12b+8b operating point (Sec. 3.5), ImplicitTerrainV2 achieves 1.23 bpp with only -0.28 dB degradation from the uncompressed model, a 3.2 \times compression ratio from float32. The reported bpp is averaged over the 50 tiles and accounts for all stored components after quantization and entropy coding, with the per-tile bpp varying primarily through the compressed size of the complexity field.

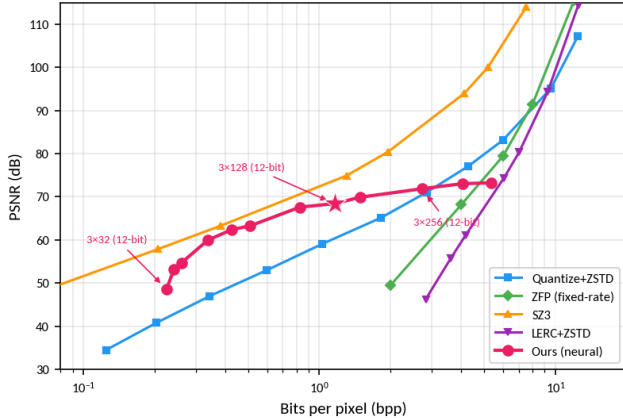


Figure 5: Rate-distortion comparison across bitrates. Red points trace our neural format as network width and depth vary under mixed-precision quantization and entropy coding, while traditional codecs are swept over their quality parameters. The \star marker denotes the configuration used throughout the other experiments. The neural format remains competitive across the full bpp range and additionally provides analytical gradients and resolution independence.

Figure 5 shows rate-distortion curves obtained by sweeping network width and depth configurations with fixed post-training quantization and entropy coding, compared against traditional codecs swept over their respective quality parameters. Across the practical bitrate range (0.5–2 bpp), the proposed neural format outperforms Quantize+ZSTD, ZFP, and LERC+ZSTD, with only SZ3 [40], an error-bounded compressor particularly suited to smooth scientific data, achieving higher PSNR at matched rates. The neural format incurs a one-time encoding cost that traditional codecs do not require, and this cost is amortized when the encoded model is queried repeatedly for analysis tasks. It provides capabilities absent from traditional codecs: continuous elevation queries at arbitrary coordinates, analytical gradient computation, and resolution-independent topological analysis. These capabilities would otherwise require separate processing pipelines on decompressed grid data.

For the model’s inference throughput, the compiled model evaluates 77.3 M coordinate queries per second on an RTX A5000, returning both elevation and gradient in a single pass. This represents a 4.63 \times speedup over naïve autograd-based gradient computation and is 2.24 \times faster than naïve elevation-only queries without compilation, indicating that the compiled analytical gradient path adds a small overhead to elevation queries. Floating-point operations (FLOPs), and memory usage are reported in Supp. C. Spatial error maps comparing the 12b+8b configuration against classical codecs on a representative tile are provided in Supp. D

4.4 Ablation Study

Table 4 isolates the contribution of each component by progressively adding them to the ImplicitTerrain-128 baseline. The first row applies an ω_0 correction at the geometry model only, from 30 to 150; the shape model retains $\omega_0 = 30$ to match the low-frequency spectrum of the Gaussian-smoothed target (Sec. 4.1). This targeted adjustment reflects the geometry stage’s distinct role of fitting a

Table 3: Storage efficiency comparison. With mixed-precision quantization and entropy coding, our neural format achieves competitive rate-distortion across the evaluated bitrates. Classical formats require a full decompression step before any query; our neural terrain format supports queries at arbitrary coordinates with analytical gradient computation, with no decompression required.

Format	bpp	PSNR (dB) \uparrow	MAE (m) \downarrow
GeoTIFF [46]+DEFLATE [11]	15.29	lossless	0
FPZIP [43]	11.78	lossless	0
LERC [14]+ZSTD [7] ($z=0.1$)	6.06	74.35	0.045
ZFP [42] (rate=4)	4.00	68.19	0.057
Quantize+ZSTD [7] (10b)	2.86	71.08	0.092
SZ3 [40] ($\epsilon=0.05$ m)	1.96	80.45	0.023
Ours (float32)	4.03	66.25	0.133
Ours (float16)	1.77	66.25	0.133
Ours (12b+8b)	1.23	65.97	0.137
Ours (int8)	1.04	61.30	0.239

Table 4: Progressive ablation from ImplicitTerrain-128 (IT-128) to ImplicitTerrainV2 (averaged over 50 tiles). Each row adds one component to the previous.

Configuration	PSNR (dB) \uparrow	Δ	Iter (ms) \downarrow
IT-128 ($\omega_0 = 30$)	49.74	—	34.5
+ ω_0 tuning	62.13	+12.39	34.4
+ FreqEmbed + GM	63.08	+0.94	34.5
+ WCF masks	65.72	+2.64	45.4
+ Adaptive sampling	66.25	+0.53	20.2

1000 \times 1000 residual dominated by high-frequency geometric detail, whereas the shape model operates at 500 \times 500 on smoothed content. The remaining three rows of Tab. 4 quantify our contributions on top of the ω_0 -tuned baseline: the improved shape model with frequency embedding and gradient matching, WCF masks at the geometry stage, and adaptive sampling. Applying the frequency embedding to the geometry model without spatial masks yields limited E2E improvement, and the embedding is retained only as a prerequisite for WCF band gating. Further analysis of mask placement and per-component overhead is provided in Supp. B and C.

4.5 Terrain Analysis Applications

Beyond fitting accuracy, a key advantage of the neural terrain format is its support for downstream terrain analysis directly from the continuous representation. Following ImplicitTerrain [23], we demonstrate two applications: topographic feature computation and topological analysis. Both operate on the shape model Ψ_s , which captures the smooth manifold structure of the terrain; topological analysis in particular requires a smooth, noise-free surface with accurate gradients, which the shape model provides by design (Tab. 2). The full elevation reconstruction $\hat{z} = \Psi_s + \Psi_g$ is used for fitting evaluation (Sec. 4.2), while the shape model alone serves as the analytical backbone for derivative-based terrain analysis.

Figure 6 visualizes the topographic quantities and the topological skeleton (*i.e.*, critical net) derived from the shape model Ψ_s on two

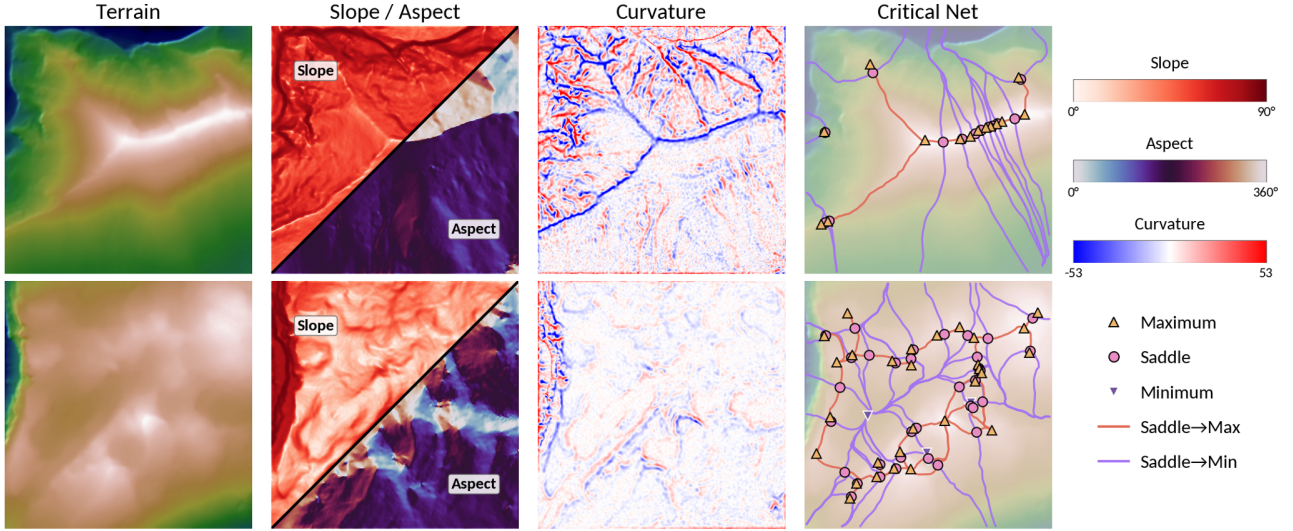


Figure 6: Topographic features and topological skeleton derived from ImplicitTerrainV2’s shape model Ψ_s via analytical gradients on two representative tiles. From left to right: elevation (DEM hillshade), combined slope and aspect (split along the anti-diagonal), mean curvature, and the critical network. Critical points (minima, maxima, saddles) are located at $\|\nabla\Psi_s\| = 0$ and classified via the Hessian eigenvalues. Separatrix lines traced by gradient delineate ridges and valleys.

representative tiles. Slope, defined as $\arctan(\|\nabla\Psi_s\|)$, and aspect, defined as $\text{atan2}(\partial\Psi_s/\partial y, \partial\Psi_s/\partial x)$, are computed from the first-order gradient $\nabla\Psi_s$. Mean curvature κ can be obtained via the standard differential geometry formula:

$$\kappa = \frac{(1 + \Psi_y^2)\Psi_{xx} - 2\Psi_x\Psi_y\Psi_{xy} + (1 + \Psi_x^2)\Psi_{yy}}{2(1 + \Psi_x^2 + \Psi_y^2)^{3/2}}. \quad (11)$$

All quantities require no grid discretization and can be evaluated at arbitrary resolution from the learned model, eliminating the resolution dependence of finite-difference operators.

For topological feature extraction, ImplicitTerrain [23] demonstrated that continuous SIREN surface models enable Morse-theoretic topological analysis. Critical points are locations where $\|\nabla\Psi_s\| = 0$; they are located using the Newton-Raphson method [32] and classified by the eigenvalues of the Hessian: both positive (minimum), both negative (maximum), or mixed signs (saddle). From each saddle, four separatrix lines are traced by integrating $\nabla\Psi_s$ (ascending toward maxima) and $-\nabla\Psi_s$ (descending toward minima), producing the Morse-Smale complex that delineates the terrain’s topological skeleton (ridges, valleys, drainage divides). ImplicitTerrainV2’s improved shape model fitting accuracy and gradient fidelity (Tab. 2) yield a more faithful topological reconstruction than the original ImplicitTerrain.

5 Conclusion

We presented ImplicitTerrainV2, a practical neural data format for terrain that encodes each DEM tile as a compact, spatially-adaptive implicit neural representation. A single stored model provides continuous coordinate queries and analytical gradients, enabling resolution-independent terrain data analysis. A wavelet complexity field concentrates model capacity in spatially complex regions, while gradient matching improves both elevation reconstruction

and gradient fidelity in the smooth shape model. Together with cascaded SIREN backbones and adaptive sampling, ImplicitTerrainV2 achieves 66.25 dB end-to-end PSNR with 124K parameters, improving over ImplicitTerrain by +5.70 dB while using 3.2× fewer parameters, 5.8× less peak GPU memory, and 4.1× faster training. After post-training quantization, the model compresses to 1.23 bpp with only 0.28 dB PSNR drop. ImplicitTerrainV2 outperforms or is on par with the evaluated traditional codecs while retaining INR’s benefit of continuous coordinate queries and analytical gradients for terrain analysis at arbitrary resolution. Experimental results demonstrate that implicit neural representations are a promising direction for compact terrain storage, combining competitive rate-distortion performance with continuous surface modeling and differentiability as native properties of the representation.

Currently, ImplicitTerrainV2 has two main limitations. First, spatially adaptive masks rely on high-frequency content being spatially sparse; their benefit over a uniform-capacity network diminishes on tiles where complex features span the full domain [21]. Second, ImplicitTerrainV2 is least accurate in nearly flat regions, a regime that is difficult because it is intrinsically ill-conditioned for gradient-based terrain analysis, where small gradient errors induce large angular errors in aspect as slope magnitude approaches zero [33]. It is also a known failure mode for neural fitting, since sinusoidal INR bases cannot cancel to a simple signal without residual oscillation. Future work includes meta-learning-based compression [13] to amortize encoding cost across tiles rather than training independently, integration with geospatial toolchains to enable practical deployment, and evaluation on other geospatial surfaces with smooth derivatives such as bathymetry and planetary DEMs.

References

- [1] Jason Ansel, Edward Yang, Horace He, Natalia Gimelshein, Animesh Jain, Michael Voznesensky, Bin Bao, Peter Bell, David Berard, Evgenii Burovski, et al. 2024.

- Pytorch 2: Faster machine learning through dynamic python bytecode transformation and graph compilation. In *Proceedings of the 29th ACM international conference on architectural support for programming languages and operating systems, volume 2*, 929–947.
- [2] Ronen Basri, Meirav Galun, Amnon Geifman, David W. Jacobs, Yoni Kasten, and Shira Kritchman. 2020. Frequency Bias in Neural Networks for Input of Non-Uniform Density. In *International Conference on Machine Learning*.
 - [3] Yizhak Ben-Shabat, Chamin Hewa Koneputugodage, Sameera Ramasinghe, and Stephen Gould. 2024. Neural experts: Mixture of experts for implicit neural representations. *Advances in Neural Information Processing Systems* 37 (2024), 101641–101670.
 - [4] Laura E. Boucheron and Charles D. Creusere. 2005. Lossless Wavelet-Based Compression of Digital Elevation Maps for Fast and Efficient Search and Retrieval. *IEEE Trans. Geosci. Remote Sens.* 43, 5 (2005), 1133–1143. doi:10.1109/TGRS.2004.841477
 - [5] Franck Cappello, Sheng Di, Sihuan Li, Xin Liang, Ali Murat Gok, Dingwen Tao, Chun Hong Yoon, Xin-Chuan Wu, Yuri Alexeev, and Frederic T. Chong. 2019. Use Cases of Lossy Compression for Floating-Point Data in Scientific Data Sets. *Int. J. High Perform. Comput. Appl.* 33, 6 (2019), 1201–1220. doi:10.1177/1094342019853336
 - [6] Yunbo Chen, Xiaojun Li, Fei Yang, and Peng Liu. 2023. BRIEF: Biomedical implicit neural representations for feature extraction. *Medical Image Analysis* 90 (2023), 102960.
 - [7] Yann Collet and Murray Kucherawy. 2018. *Zstandard Compression and the 'application/zstd' Media Type*. RFC RFC 8478. Internet Engineering Task Force (IETF). doi:10.17487/RFC8478
 - [8] Wojciech M Czarnecki, Simon Osindero, Max Jaderberg, Grzegorz Swirszcz, and Razvan Pascanu. 2017. Sobolev training for neural networks. *Advances in neural information processing systems* 30 (2017).
 - [9] Adam Dai, Shubh Gupta, and Grace Gao. 2024. Neural elevation models for terrain mapping and path planning. *arXiv preprint arXiv:2405.15227* (2024).
 - [10] Leila De Floriani, Ulderico Fugacci, Federico Iuricich, and Paola Magillo. 2015. Morse complexes for shape segmentation and homological analysis: discrete models and algorithms. In *Computer graphics forum*, Vol. 34. Wiley Online Library, 761–785.
 - [11] Peter Deutsch. 1996. *DEFLATE Compressed Data Format Specification version 1.3*. RFC RFC 1951. Internet Engineering Task Force (IETF). doi:10.17487/RFC1951
 - [12] Emilien Dupont, Adam Goliński, Milad Alizadeh, Yee Whye Teh, and A. Doucet. 2021. COIN: C-Compression with Implicit Neural representations. *ArXiv abs/2103.03123* (2021).
 - [13] Emilien Dupont, Hrushikesh Loya, Milad Alizadeh, Adam Goliński, Yee Whye Teh, and Arnaud Doucet. 2022. Coin++: Neural compression across modalities. *arXiv preprint arXiv:2201.12904* (2022).
 - [14] Esri. 2024. LERC: Limited Error Raster Compression. <https://github.com/Esri/lerc>. Accessed: 2026-04-16.
 - [15] Amer Essakine, Yanqi Cheng, Chun-Wun Cheng, Lipai Zhang, Zhongying Deng, Lei Zhu, Carola-Bibiane Schönlieb, and Angelica I Aviles-Rivero. 2024. Where Do We Stand with Implicit Neural Representations? A Technical and Performance Survey. *arXiv preprint arXiv:2411.03688* (2024).
 - [16] Morsali et al. 2025. STAF: Sinusoidal Trainable Activation Functions for Implicit Neural Representation. *arXiv* (2025).
 - [17] Rizal Fathony, Anit Kumar Sahu, Devin Willmott, and J Zico Kolter. 2020. Multi-convolutional filter networks. In *International Conference on Learning Representations*.
 - [18] Riccardo Fellegara, Federico Iuricich, and Leila De Floriani. 2017. Efficient representation and analysis of triangulated terrains. In *Proceedings of the 25th ACM SIGSPATIAL International Conference on Advances in Geographic Information Systems*, 1–4.
 - [19] Riccardo Fellegara, Federico Iuricich, Yunting Song, and Leila De Floriani. 2023. Terrain trees: a framework for representing, analyzing and visualizing triangulated terrains. *Geoinformatica* 27, 3 (2023), 525–564.
 - [20] Riccardo Fellegara, Federico Iuricich, Leila De Floriani, and Kenneth Weiss. 2014. Efficient computation and simplification of discrete Morse decompositions on triangulated terrains. In *Proceedings of the 22nd ACM SIGSPATIAL International Conference on Advances in Geographic Information Systems*, 223–232.
 - [21] Haoan Feng, Diana Aldana, Tiago Novello, and Leila De Floriani. 2025. SAS-Net: Spatially-adaptive sinusoidal neural networks for INRs. *arXiv preprint arXiv:2503.09750* (2025).
 - [22] Haoan Feng, Yunting Song, and Leila De Floriani. 2024. Critical features tracking on triangulated irregular networks by a scale-space method. In *Proceedings of the 32nd ACM International Conference on Advances in Geographic Information Systems*, 54–66.
 - [23] Haoan Feng, Xin Xu, and Leila De Floriani. 2024. ImplicitTerrain: a Continuous Surface Model for Terrain Data Analysis. In *Proceedings of the IEEE/CVF Conference on Computer Vision and Pattern Recognition Workshop*, 899–909.
 - [24] Robin Forman. 1998. Morse theory for cell complexes. *Advances in mathematics* 134, 1 (1998), 90–145.
 - [25] Robin Forman. 2002. A user's guide to discrete Morse theory. *Séminaire Lotharingien de Combinatoire* 48 (2002), B48c.
 - [26] Ulderico Fugacci, Sara Scaramuccia, Federico Iuricich, Leila De Floriani, et al. 2016. Persistent Homology: a Step-by-step Introduction for Newcomers.. In *STAG*, 1–10.
 - [27] Michael Garland and Paul S. Heckbert. 1995. Fast Triangular Approximation of Terrains and Height Fields. In *Technical Report CMU-CS-95-181*. Carnegie Mellon University.
 - [28] Amir Gholami, Sehoon Kim, Zhen Dong, Zhewei Yao, Michael W Mahoney, and Kurt Keutzer. 2022. A survey of quantization methods for efficient neural network inference. In *Low-power computer vision*. Chapman and Hall/CRC, 291–326.
 - [29] Amos Gropp, Lior Yariv, Niv Haim, Matan Atzmon, and Yaron Lipman. 2020. Implicit geometric regularization for learning shapes. *arXiv preprint arXiv:2002.10099* (2020).
 - [30] Zekun Hao, Arun Mallya, Serge Belongie, and Ming-Yu Liu. 2022. Implicit Neural Representations with Levels-of-Experts. *Advances in Neural Information Processing Systems* 35 (2022), 2564–2576.
 - [31] Amir Hertz, Or Perel, Raja Giryes, Olga Sorkine-Hornung, and Daniel Cohen-Or. 2021. Sape: Spatially-adaptive progressive encoding for neural optimization. *Advances in Neural Information Processing Systems* 34 (2021), 8820–8832.
 - [32] Francis Begnaud Hildebrand. 1987. *Introduction to numerical analysis*. Courier Corporation.
 - [33] Berthold K. P. Horn. 1981. Hill shading and the reflectance map. *Proc. IEEE* 69, 1 (1981), 14–47.
 - [34] Amirhossein Kazerouni, Reza Azad, Alireza Hosseini, Dorit Merhof, and Ulas Bagci. 2024. INCODE: Implicit Neural Conditioning with Prior Knowledge Embeddings. In *Proceedings of the IEEE/CVF Winter Conference on Applications of Computer Vision*, 1298–1307.
 - [35] David B. Kidner and Derek H. Smith. 2003. Advances in the Data Compression of Digital Elevation Models. *Comput. Geosci.* 29, 8 (2003), 985–1002. doi:10.1016/S0098-3004(03)00097-9
 - [36] Diederik P Kingma and Jimmy Ba. 2014. Adam: A method for stochastic optimization. *arXiv preprint arXiv:1412.6980* (2014).
 - [37] Théo Ladune, Pierrick Philippe, Félix Henry, Erwan Le Penneç, and Clare E. Gordon. 2023. Cool-chic: Coordinate-based Low Complexity Hierarchical Image Codec. In *IEEE International Conference on Computer Vision (ICCV)*.
 - [38] Shaomeng Li, Peter Lindstrom, and John Clyne. 2023. Lossy Scientific Data Compression With SPERR. In *Proc. IEEE Int. Parallel Distrib. Process. Symp. (IPDPS)*, 1007–1017. doi:10.1109/IPDPS54959.2023.00104
 - [39] Zhilin Li, Qing Zhu, and Christopher Gold. 2004. *Digital Terrain Modeling: Principles and Methodology*. CRC Press.
 - [40] Xin Liang, Kai Zhao, Sheng Di, Sihuan Li, Robert Underwood, Ali M Gok, Jiannan Tian, Junjing Deng, Jon C Calhoun, Dingwen Tao, et al. 2022. Sz3: A modular framework for composing prediction-based error-bounded lossy compressors. *IEEE Transactions on Big Data* 9, 2 (2022), 485–498.
 - [41] David B Lindell, Dave Van Veen, Jeong Joon Park, and Gordon Wetzstein. 2022. Bacon: Band-limited coordinate networks for multiscale scene representation. In *Proceedings of the IEEE/CVF Conference on Computer Vision and Pattern Recognition*, 16252–16262.
 - [42] Peter Lindstrom. 2014. Fixed-Rate Compressed Floating-Point Arrays. *IEEE Trans. Vis. Comput. Graph.* 20, 12 (2014), 2674–2683. doi:10.1109/TVCG.2014.2346458
 - [43] Peter Lindstrom and Martin Isenburg. 2006. Fast and Efficient Compression of Floating-Point Data. *IEEE Trans. Vis. Comput. Graph.* 12, 5 (2006), 1245–1250. doi:10.1109/TVCG.2006.143
 - [44] Jinyang Liu, Sheng Di, Kai Zhao, Xin Liang, Sian Jin, Zizhe Jian, Jiajun Huang, Shixun Wu, Zizhong Chen, and Franck Cappello. 2024. High-Performance Effective Scientific Error-Bounded Lossy Compression with Auto-Tuned Multi-Component Interpolation. *Proc. ACM Manag. Data* 2, 1 (2024), 1–27. doi:10.1145/3639259
 - [45] Zhen Liu, Hao Zhu, Qi Zhang, Jingde Fu, Weibing Deng, Zhan Ma, Yanwen Guo, and Xun Cao. 2024. FINER: Flexible spectral-bias tuning in Implicit Neural Representation by Variable-periodic Activation Functions. In *Proceedings of the IEEE/CVF Conference on Computer Vision and Pattern Recognition*, 2713–2722.
 - [46] Sk Sazid Mohammad and R Ramakrishnan. 2003. GeoTIFF-A standard image file format for GIS applications. *Map India* (2003), 28–31.
 - [47] Shishira R. Maiya, Max Ehrlich, Hanlin Kim, Jiaqi Ren, Lingjie Li, and Kfir Aberman. 2023. NIRVANA: Neural Implicit Representations of Videos with Adaptive Networks and Autoregressive Patching. *arXiv preprint arXiv:2212.14593* (2023).
 - [48] Stephane G. Mallat. 1989. A theory for multiresolution signal decomposition: the wavelet representation. *IEEE Trans. Pattern Anal. Mach. Intell.* 11, 7 (1989), 674–693. doi:10.1109/34.192463
 - [49] Julien NP Martel, David B Lindell, Connor Z Lin, Eric R Chan, Marco Monteiro, and Gordon Wetzstein. 2021. Acorn: Adaptive coordinate networks for neural scene representation. *arXiv preprint arXiv:2105.02788* (2021).
 - [50] Ishit Mehta, Michaël Gharbi, Connelly Barnes, Eli Shechtman, Ravi Ramamoorthi, and Manmohan Chandraker. 2021. Modulated periodic activations for generalizable local functional representations. In *Proceedings of the IEEE/CVF International Conference on Computer Vision*, 14214–14223.

- [51] Paulius Micekevicius, Sharan Narang, Jonah Alben, Gregory Diamos, Erich Elsen, David Garcia, Boris Ginsburg, Michael Houston, Oleksii Kuchaiev, Ganesh Venkatesh, et al. 2017. Mixed precision training. *arXiv preprint arXiv:1710.03740* (2017).
- [52] John Willard Milnor. 1963. *Morse theory*. Number 51. Princeton university press.
- [53] Thomas Müller, Alex Evans, Christoph Schied, and Alexander Keller. 2022. Instant neural graphics primitives with a multiresolution hash encoding. *ACM Transactions on Graphics* 41, 4 (2022), 1–15.
- [54] Guy P. Nason and Bernard W. Silverman. 1995. The Stationary Wavelet Transform and Some Statistical Applications. In *Wavelets and Statistics*. Springer New York, 281–299. doi:10.1007/978-1-4612-2544-7_17
- [55] Tiago Novello, Diana Aldana, Andre Araujo, and Luiz Velho. 2025. Tuning the Frequencies: Robust Training for Sinusoidal Neural Networks. arXiv:2407.21121 [cs.LG] <https://arxiv.org/abs/2407.21121>
- [56] Tiago Novello, Guilherme Schardong, Luiz Schirmer, Vinícius da Silva, Hélio Lopes, and Luiz Velho. 2022. Exploring differential geometry in neural implicits. *Computers & Graphics* 108 (2022), 49–60. doi:10.1016/j.cag.2022.09.003
- [57] Alan V Oppenheim. 1999. *Discrete-time signal processing*. Pearson Education India.
- [58] Nasim Rahaman, Aristide Baratin, Devansh Arpit, Felix Dräxler, Min Lin, Fred A. Hamprecht, Yoshua Bengio, and Aaron C. Courville. 2018. On the Spectral Bias of Neural Networks. In *International Conference on Machine Learning*.
- [59] Sameera Ramasinghe, Lachlan E MacDonald, and Simon Lucey. 2022. On the frequency-bias of coordinate-mlps. *Advances in Neural Information Processing Systems* 35 (2022), 796–809.
- [60] Vishwanath Saragadam, Daniel LeJeune, Jasper Tan, Guha Balakrishnan, Ashok Veeraraghavan, and Richard G Baraniuk. 2023. Wire: Wavelet implicit neural representations. In *Proceedings of the IEEE/CVF Conference on Computer Vision and Pattern Recognition*. 18507–18516.
- [61] Vishwanath Saragadam, Jasper Tan, Guha Balakrishnan, Richard G Baraniuk, and Ashok Veeraraghavan. 2022. MINER: Multiscale Implicit Neural Representations. In *European Conference on Computer Vision*.
- [62] Sara Scaramuccia, Federico Iuricich, Leila De Floriani, and Claudia Landi. 2020. Computing multiparameter persistent homology through a discrete Morse-based approach. *Computational Geometry* 89 (2020), 101623.
- [63] Kexuan Shi, Xingyu Zhou, and Shuhang Gu. 2024. Improved Implicit Neural Representation with Fourier Reparameterized Training. In *Proceedings of the IEEE/CVF Conference on Computer Vision and Pattern Recognition*. 25985–25994.
- [64] Vincent Sitzmann, Julien Martel, Alexander Bergman, David Lindell, and Gordon Wetzstein. 2020. Implicit neural representations with periodic activation functions. *Advances in Neural Information Processing Systems* 33 (2020), 7462–7473.
- [65] Swisstopo. 2023. SwissALTI3D datasets. <https://www.swisstopo.admin.ch/en/height-model-swissalti3d>.
- [66] Matthew Tancik, Pratul Srinivasan, Ben Mildenhall, Sara Fridovich-Keil, Nithin Raghavan, Utkarsh Singhal, Ravi Ramamoorthi, Jonathan Barron, and Ren Ng. 2020. Fourier features let networks learn high frequency functions in low dimensional domains. *Advances in Neural Information Processing Systems* 33 (2020), 7537–7547.
- [67] Dingwen Tao, Sheng Di, Xin Liang, Zizhong Chen, and Franck Cappello. 2019. Optimizing Lossy Compression Rate-Distortion from Automatic Online Selection between SZ and ZFP. *IEEE Trans. Parallel Distrib. Syst.* 30, 8 (2019), 1763–1777. doi:10.1109/TPDS.2019.2894404
- [68] Thomas Walker, Octave Mariotti, Amir Vaxman, and Hakan Bilen. 2025. Spatially-Adaptive Hash Encodings for Neural Surface Reconstruction. In *2025 IEEE/CVF Winter Conference on Applications of Computer Vision (WACV)*. IEEE, 2963–2972.
- [69] Ian H Witten, Radford M Neal, and John G Cleary. 1987. Arithmetic coding for data compression. *Commun. ACM* 30, 6 (1987), 520–540.
- [70] Zhongyi Xie, W. Randolph Franklin, and Daniel M. Tracy. 2010. Slope Preserving Lossy Terrain Compression. *ACM SIGSPATIAL Special* 2, 1 (2010), 19–24. doi:10.1145/1953102.1953106
- [71] Wentao Yuan, Qingtian Zhu, Xiangyue Liu, Yikang Ding, Haotian Zhang, and Chi Zhang. 2022. Sobolev training for implicit neural representations with approximated image derivatives. In *European Conference on Computer Vision*. Springer, 72–88.
- [72] Gizem Yüce, Guillermo Ortiz-Jiménez, Beril Besbinar, and Pascal Frossard. 2022. A structured dictionary perspective on implicit neural representations. In *Proceedings of the IEEE/CVF Conference on Computer Vision and Pattern Recognition*. 19228–19238.
- [73] Lyle W. Zevenbergen and Colin R. Thorne. 1987. Quantitative analysis of land surface topography. *Earth Surface Processes and Landforms* 12, 1 (1987), 47–56.

A Dataset Curation

We evaluate on 50 terrain tiles selected from 33,399 candidates from the swissALTI3D DEM [65] via a two-pass pipeline. Each raw tile covers 2000×2000 pixels at 0.5 m resolution, which we downsample to 1000×1000 (1 m) for training. *Pass 1 (quality)* computes texture and frequency descriptors on 256×256 versions (~ 17 ms/tile) and rejects tiles with missing data, elevation range below 50 m, near-zero surface variation, or more than 70% low-gradient pixels (32,937 of 33,399 accepted). *Pass 2 (diversity)* computes a 10-dimensional descriptor (elevation range, normalized std, mean and 95th-percentile gradient, low-gradient ratio, high-frequency spectral energy, 90th/95th-percentile frequencies, spectral slope, Haar-wavelet complexity), z-score normalizes the features, and applies greedy farthest-point sampling (seed = 42). The 50 selected tiles span gentle valleys (21 tiles, < 200 m elevation range), hilly foothills (19 tiles, 200–500 m), and alpine terrain (10 tiles, > 500 m, up to 1,667 m), with absolute elevations 101–1,668 m (mean 339 m), wavelet complexity 0.33–0.86, and low-gradient ratio 0.06–0.70. For preprocessing, each tile is bilinearly downsampled to 1000×1000 as the geometry-model ground truth. The shape-model target additionally normalizes to $[0, 1]$, Gaussian-smooths, and downsamples to 500×500 . Each tile is independently fitted by the INR with its own weights.

B Hidden Layer Mask Ablation

The original SASNet [21] applies spatial masks to both the input layer and all hidden layers (8 neuron groups per hidden layer), a design motivated by RGB image fitting, where repeated textures benefit from location-conditioned gating throughout the network. To test whether this carries over to terrain, we run SASNet with a hash-grid encoder ($\omega_0=150$, 2,000 iterations) on 5 tiles that span the dataset’s complexity range. Enabling hidden-layer masks *degrades* geometry-model PSNR by 0.58 dB on average (40.17 dB without vs. 39.59 dB with), with per-tile drops ranging from 0.13 to 1.05 dB. The hidden-layer mask decoders add only 1,176 parameters (+1.3%), so the degradation is not driven by reduced capacity but more likely by group-level gating in the hidden SIREN layers, limiting cross-group feature interaction, which is unhelpful for smooth, spatially non-repetitive terrain residuals. In this ablation, input-layer spatial adaptivity alone (selecting which frequency bands are active at each location) performs best, motivating our design choice to apply WCF masks only at the first layer.

C Efficiency, Training, and Numerical Analysis

Gradient matching (GM) overhead. GM computes $\partial f / \partial \mathbf{x}$ via PyTorch autograd on a 10K-pixel random subsample of the 500×500 shape grid drawn each iteration, and matches against finite-difference ground-truth gradients. On the shape model, it adds +7.8% peak memory (1,243 to 1,340 MB) and +11.8% per-iteration time (17.96 to 20.07 ms), nearly tile-independent (± 0.04 ms std) and dominated by autograd overhead. Since GM runs only during the 3,000-iteration shape phase, end-to-end pipeline overhead is +5.0%, and the 10K subsample reduces measured GM FLOPs by $16.5\times$ vs. full-grid gradient computation, with no observed change in our metrics.

WCF and adaptive sampling (AS). For the geometry model on a 1000×1000 tile under `torch.compile+AMP`, the WCF decoder adds

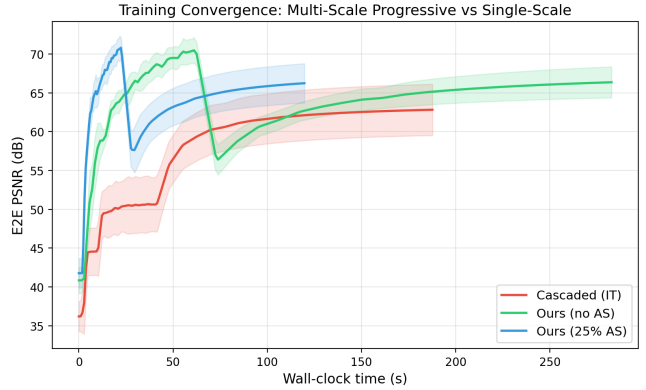


Figure 1: Convergence on 5 tiles: our single-scale WCF pipeline with 25% AS (green) reaches higher E2E PSNR faster than cascaded pyramid baseline [23] (blue).

+15.6 ms per iteration (+50.8% over a 30.6 ms SIREN baseline), 14% less than the hash-grid alternative (+59.2%), and uses 14.6K fewer mask parameters (24K vs. 39K). With 25% complexity-guided AS, the full WCF+AS pipeline runs at 20.2 ms per iteration (-34.1% vs. SIREN baseline at matched iterations): the $4\times$ pixel reduction dominates the decoder cost. Peak GPU memory drops from 5.9 GB to 1.8 GB ($3.2\times$ reduction).

Multi-scale vs. single-scale training. ImplicitTerrain [23] trains its shape model using Gaussian pyramid progressive training (coarse-to-fine resolutions). As shown in Fig 1, on 5 randomly selected tiles and under matched iteration budgets (3,000 shape + 2,000 geometry) with the same 3×128 backbone and GM, our single-scale pipeline with WCF reaches 66.39 ± 2.00 dB E2E PSNR vs. 62.83 ± 3.30 dB for the cascaded pyramid, and with 25% AS reaches 66.25 ± 2.53 dB (+3.42 dB over the pyramid) at $1.57\times$ faster wall-clock time (120.6 vs. 189.4 s, full-precision protocol shared with ImplicitTerrain).

Shape-model sampling. Because the shape target is Gaussian-smoothed (low-frequency), uniform subsampling reduces cost with negligible quality change. On 10 tiles, both 50% and 25% uniform subsampling lose only -0.01 dB PSNR with unchanged GradMAE to four decimals, providing $1.27\times$ and $1.84\times$ speedups. At 25%, ~ 62.5 K pixels still exceed the model’s 50K parameters, and the smooth signal is spatially redundant. The geometry model, by contrast, requires complexity-guided sampling because its residual is spatially non-uniform. We adopt 25% uniform subsampling as the default for shape-model training.

Profiling. All 128-width methods share an identical 50K-parameter SIREN backbone per stage, differing only in auxiliary modules, while the cascaded baseline uses a 3×256 backbone (198K/stage, no auxiliary). SASNet adds a 39K hash-grid mask branch in the geometry stage, whereas our WCF decoder uses 24K, saving 14.6K auxiliary parameters while achieving higher accuracy. Per-query forward FLOPs are 99K ($1.00\times$) for SIREN-128, 101K ($1.02\times$) for SASNet hash-grid, 147K ($1.49\times$) for WCF, and 395K ($3.98\times$) for the 3×256 baseline. The $4\times$ pixel reduction from AS yields a net $2.25\times$ training speedup despite the higher per-query cost. Per-stage peak GPU memory (shape/geometry) is 1,340/1,740 MB for ours vs.

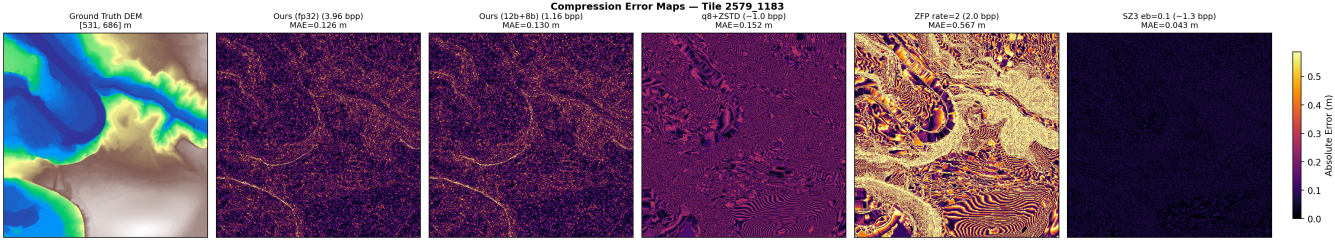


Figure 2: Absolute-error maps on a tile with 155 m relief (shared colorscale in m).

2,464/9,800 for the 3×256 baseline and 1,241/5,436 for SASNet, and AS makes our geometry stage comparable to the shape stage. The deployed artifact stores the 100K-parameter SIREN backbone plus the 24K WCF decoder, scales, learned thresholds, normalization statistics, and a 4-bit, entropy-coded low-resolution complexity field, all counted toward the reported 1.23 bpp (averaged across 50 tiles, since the compressed complexity field varies by tile). At inference, the normalized complexity field \hat{c} at each query coordinate is obtained by bilinear interpolation of the decoded low-resolution field, and the $K=4$ band masks are then produced via the learned thresholds, matching the pathway used during training.

Inference and numerical notes. On an RTX A5000 (50 warmup + 200 timed iterations), the compiled analytical-gradient path reaches 77.3 Mq/s at 1M-query batch and saturates beyond 100K queries, a 2.24 \times speedup over naïve elevation-only (34.6 Mq/s), so the optimized path returns elevation *and* gradient faster than the unoptimized path returns elevation alone, due to `torch.compile` fusing `sin/cos/matmul` kernels and AMP halving memory bandwidth. End-to-end training takes 55 s/tile with `torch.compile+AMP`, covering the cascaded shape phase (3,000 iterations) and geometry phase (2,000 iterations at WCF + 25% AS). Native float16 SIREN training produces NaN on all tested tiles because the $\sin(\omega_0 \mathbf{W}\mathbf{x}+\mathbf{b})$ activation accumulates rounding error through 3 hidden layers that exceeds the signal amplitude. AMP (forward in float16, master weights in float32, with gradient scaling) matches float32 to within 0.01 dB at 1.94 \times speedup.

D Compression and Rate-distortion Analysis

Per-layer quantization sensitivity. We sweep per-layer PSNR drop when quantizing each layer group individually with all others at float32, using weight-only symmetric uniform quantization with per-output-channel weight scales and 16-bit biases. Input-layer weights are regenerable from the frequency table and skipped in the deployed format, with sensitivity values reported only for reference. Table 1 reports Δ PSNR for both stages. Two patterns emerge. First, sensitivity decreases from input to output layers, since input-layer perturbations are amplified by ω_0 through subsequent sine activations. Second, the shape model ($\omega_0=30$) is substantially more sensitive than the geometry model ($\omega_0=150$) at the same bit-width, because the geometry model fits simpler residual signals with smaller weight magnitudes. The WCF decoder is nearly insensitive since it produces binary masks robust to perturbations. At 12-bit, all shape-model layers stay within -0.83 dB and all geometry-model

Table 1: Per-layer quantization sensitivity: Δ PSNR (dB) when quantizing one layer group with others at float32. Shape baseline 68.37 dB, geometry baseline 44.52 dB.

Stage	Layer	16b	12b	10b	8b
Shape	Input	-0.00	-0.83	-5.69	-17.69
	Hidden 0	+0.00	-0.03	-1.47	-8.60
	Hidden 1	-0.00	-0.04	-0.83	-6.36
	Hidden 2	+0.00	+0.00	-0.09	-1.61
	Output	-0.00	-0.00	-0.19	-1.78
Geometry	Input	-0.00	-0.04	-0.52	-5.26
	Hidden 0	-0.00	-0.01	-0.16	-2.05
	Hidden 1	-0.00	-0.00	-0.05	-0.87
	Hidden 2	-0.00	-0.00	-0.01	-0.11
	Output	-0.00	-0.00	-0.00	-0.00
	WCF dec.	+0.00	-0.00	-0.00	-0.03

layers within -0.04 dB, motivating the mixed-precision configuration: 12-bit for the shape model (preserving gradient accuracy) and 8-bit for the geometry model and WCF decoder, yielding 1.23 bpp at only -0.28 dB E2E across 50 tiles.

QAT vs. PTQ. On 5 tiles, QAT with a straight-through estimator gives negligible improvement at int8 (+0.02 dB, 60.87 vs. 60.85) while substantially degrading float32 quality (-4.52 dB, 61.29 vs. 65.81): fake-quantization noise during training appears to hinder the model from learning fine spatial details. At our 12b+8b target operating point, QAT also underperforms PTQ (61.19 vs. 65.54), because 12-bit PTQ already incurs only small loss on the standard-trained model. We hypothesize that SIREN’s frequency amplification $\sin(\omega_0 \mathbf{W}\mathbf{x}+\mathbf{b})$, which magnifies weight perturbations by ω_0 , creates a precision floor at 8-bit that is difficult to overcome through training-time optimization alone. QAT narrows the float32-to-int8 gap (from -4.96 to -0.42 dB) by lowering the float32 ceiling rather than raising the int8 floor. We therefore adopt PTQ for the neural terrain format, as QAT adds training complexity without measurable benefit at the target bit-widths.

Compression error maps. Fig. 2 visualizes spatial error distributions on a representative steep-foothills tile. On this illustrative tile, our 12b+8b configuration reaches MAE/MaxAE of 0.130 m / 6.02 m, vs. q8+ZSTD at 0.152 m / 0.31 m, ZFP rate=2 (2.0 bpp) at 0.567 m / 49.14 m, and SZ3 ($\epsilon=0.1$, ~ 1.3 bpp) at 0.043 m / 0.10 m. Neural errors concentrate at complex features (ridgelines, cliff edges, steep slopes) and stay small in flat regions, so worst cases occur at spatially predictable locations rather than scattered across smooth regions.